Effect of Ce Doping of a Co/Al_2O_3 Catalyst on Hydrogen Production via Propane Steam Reforming

Jeong Yeon Do [1], Rama Krishna Chava [1], Namgyu Son [1], Junyeong Kim [1], No-Kuk Park [2], Doyeon Lee [3], Myung Won Seo [3], Ho-Jung Ryu [3], Jun Hwa Chi [4] and Misook Kang [1,*]

[1] Department of Chemistry, College of Science, Yeungnam University, Gyeongsan, Gyeongbuk 38541, Korea; daengi77@ynu.ac.kr (J.Y.D.); ramakrishna911@gmail.com (R.K.C.); sng1107@ynu.ac.kr (N.S.); jjun@ynu.ac.kr (J.K.)

[2] School of Chemical Engineering, Yeungnam University, Gyeongsan, Gyeongbuk 38541, Korea; nokukpark@ynu.ac.kr

[3] Korea Institute of Energy Research, 152 Gajeong-ro, Yuseong-gu, Daejeon 34129, Korea; dylee82@kier.re.kr (D.L.); mwseo82@kier.re.kr (M.W.S.); hjryu@kier.re.kr (H.-J.R.)

[4] Korea Electric Power Corporation Research Institute, 105 Munji-ro, Yuseong-gu, Daejeon 34056, Korea; jhchi@kepco.co.kr

* Correspondence: mskang@ynu.ac.kr; Tel.: +82-53-810-2363; Fax: +82-53-815-5412

Abstract: We synthesized cerium-doped cobalt-alumina (Co_xCe_y/Al_2O_3) catalysts for the propane steam reforming (PSR) reaction. Adding cerium introduces oxygen vacancies, and the oxygen transfer capacity of the Ce promoter favors CO to CO_2 conversion during PSR, inhibiting coke deposition and promoting hydrogen production. The best PSR activity was achieved at 700 °C using the $Co_{0.85}Ce_{0.15}/Al_2O_3$ catalyst, which showed 100% propane (C_3H_8) conversion and about 75% H_2 selectivity, and 6% CO, 5% CO_2, and 4% CH_4 were obtained. In contrast, the H_2 selectivity of the base catalyst, Co/Al_2O_3, is 64%. The origin of the difference in activity was the lower C_3H_8 gas desorption temperature of the $Co_{0.85}Ce_{0.15}/Al_2O_3$ catalyst compared to that of the Co/Al_2O_3 catalyst; thus, the PSR occurred at low temperatures. Furthermore, more CO was adsorbed on the $Co_{0.85}Ce_{0.15}/Al_2O_3$ catalyst, and subsequently, desorbed as CO_2. The activation energy for water desorption from the $Co_{0.85}Ce_{0.15}/Al_2O_3$ catalyst was 266.96 kJ/mol, higher than that from Co/Al_2O_3. Furthermore, the water introduced during the reaction probably reacted with CO on the $Co_{0.85}Ce_{0.15}/Al_2O_3$ catalyst, increasing CO_2 generation. Finally, we propose a mechanism involving the $Co_{0.85}Ce_{0.15}/Al_2O_3$ catalyst, wherein propane is reformed on Co_xCe_y sites, forming H_2, and CO, followed by the conversion of CO to CO_2 by water on CeO_2 sites.

Keywords: Propane steam reforming; Hydrogen production; Co_xCe_y/Al_2O_3; CO desorption; oxygen vacancies

1. Introduction

At the Davos World Economic Forum in January 2017, a hydrogen consortium was formed consisting of chief executive officers from major companies in Asia, Europe, and the United States of America, as well as national policy makers. At the Sustainability Innovation Forum in November 2017, the hydrogen consortium predicted that the demand for hydrogen fuel cell vehicles would increase from 10 to 15 million cars by 2030 and to 500,000 trucks by 2030. Moreover, the demand for hydrogen is expected to expand to 10 times its current level because of its wide use in other industries [1]. Thus, the era of the hydrogen economy has arrived. The increasing use of hydrogen energy will help protect the environment, although it may not represent the next-generation energy revolution. Methods for producing hydrogen from hydrocarbons include catalytic cracking [2], catalytic partial

oxidation [3], carbon dioxide reforming [4], and steam catalytic reforming [5]. Without considering the CO_2 separation, treatment, and storage steps, the steam catalytic reforming process has been evaluated as the most economical large-scale hydrogen production process and has already been commercialized. The economic efficiency of these processes can be evaluated based on the raw material composition of the supplied hydrocarbon gas and the final consumption and destination of the produced synthesis gas. In addition, because CO_2 emission regulations are becoming stricter, the cost of CO_2 disposal will exert a significant impact on the overall economic assessment. In the steam reforming (SR) process, steam is added to a hydrocarbon (here, propane steam reforming or PSR), resulting in the decomposition of the hydrocarbon, as shown in Equation (1) [6].

$$C_3H_8 + 6H_2O \rightarrow 3CO_2 + 10H_2, \Delta H_{298} = 499 \text{ kJ/mol} \tag{1}$$
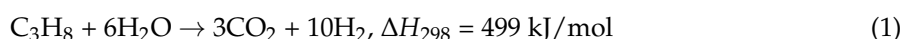
The CO_2/H_2 ratio of the product gas is 0.3, which is lower than that of the partial oxidation process, and it is advantageous in that a larger amount of hydrogen can be obtained from a small amount of hydrocarbon. However, the PSR process has a disadvantage: It requires a high water vapor/carbon ratio of over six to prevent coke formation on the catalyst. In addition, the process consumes a large amount of energy because the process temperature is as high as 800 °C. The entire SR process is now briefly described [7] and is divided into pretreatment and posttreatment processes based on the use of a steam reformer. In the pretreatment process, a hydrogen desulfurization system (HDS) and a prereformer are installed. In the posttreatment step, there is a high-temperature shift (HTS) reactor, a low-temperature shift (LTS) reactor, a CO_2 separator, and a methanation reactor. As parts of the CO_2 separation device, a conventional absorption device and a pressure swing adsorption (PSA) device for increasing the separation efficiency are used. In particular, the final section of the hydrocarbon reformer system must purify the raw hydrogen. In modern plants, a PSA unit is used to achieve the final product purity. In this process, the separated carbon dioxide can be collected and used for various purposes without being disposed of in the atmosphere. In particular, carbon capture and utilization (CCU) devices are attractive, and the reduction of carbon dioxide by hydrogen (thermal reaction) or water (photoreaction) to convert it into fuel or to other high-value chemicals is one such application. However, in this paper, only the main process, steam reforming, is discussed. Cobalt [8] and nickel [9] catalysts are widely used in the PSR process. Precious metal catalysts such as Rh show low carbon deposition, but are not used for economic reasons [10]. Nickel has a sintering temperature of 590 °C, which is lower than the process temperature of the steam catalytic reaction (600–800 °C); therefore, nickel is usually dispersed and supported on a carrier such as Al_2O_3, KOH, MgO, or urania. The carrier is added to promote the gasification of the carbon on the catalyst surface. As the catalytic species can evaporate at high temperatures, they are added in the form of potassium alumina-silicates or calcium magnesia silicates, for example, $NiO/K-Al_2O_3$, $NiO/Al_2O_3/CaO$, and $NiO/MgAl_2O_4$ [11–13]. Many researchers have reported that NiC formation is suppressed by the steam reforming of catalysts loaded with promoters such as Pt, Ir, Sn, Pb, Ge, As, Sb, Bi, Ag, Cu, and Zn [14–20].

Previously, we have confirmed that the deposition of coke on the Co–Mn catalyst is lower than that on other catalysts and hydrogen production is close to 75% [21]. Furthermore, we have shown that, in the Co/Mn catalyst, the oxygen vacancies of the manganese oxides are well supplied with oxygen for the reforming of propane on the cobalt sites, enabling the reforming reaction to occur continuously. However, a promoter with greater oxygen transfer capability is required to confirm this effect. Therefore, in this study, cobalt was selected as a main catalyst and another metal catalyst for promoting oxygen vacancies, which was added as a catalytic promoter. However, in the PSR process, the deterioration of the catalyst because of carbon deposition on the catalyst surface is a major obstacle to commercial use. Therefore, generally, in the steam reforming process, excess steam is added to prevent carbon deposition. Carbon deposition on the catalyst is produced in the form of encapsulating coke and whisker-like coke [22]. The encapsulating coke reduces catalyst activity, and the whisker coke increases catalyst sintering, which eventually blocks the movement of the reactant gas, and thus, increases the pressure differential in the reactor. In both cases, however, these factors contribute to

reduce the activity of the catalyst. On the other hand, the deposition of encapsulating coke is somewhat related to the CO generated in the steam reforming reaction [23]. Therefore, it is possible to control the encapsulating coke deposition if the amount of CO adsorbed on the catalyst surface is reduced by converting the produced CO into CO_2 during the reaction. Furthermore, the water gas shift (WGS) of CO can assist in the production of hydrogen, as shown by Equation (2):

$$CO + H_2O \rightarrow CO_2 + H_2. \tag{2}$$

In this study, we used ceria as a co-catalyst, expecting it to play a role as an oxidation catalyst to convert CO to CO_2 [24]. The aim of this study is to suppress the deterioration of the catalyst by converting the CO gas generated during the PSR reaction to CO_2 by using the lattice oxygen of Ce_xO_y, which was used as a promoter to achieve higher hydrogen production over the Co-based catalyst. A catalyst loaded with 30% cobalt oxide on 70% γ-Al_2O_3 was used as the base catalyst, and four kinds of cerium-doped catalysts were prepared: $30Co_{0.97}Ce_{0.03}/70\gamma$-$Al_2O_3$, $30Co_{0.85}Ce_{0.15}/70\gamma$-$Al_2O_3$, $30Co_{0.79}Ce_{0.21}/70\gamma$-$Al_2O_3$, and $30Co_{0.70}Ce_{0.30}/70\gamma$-$Al_2O_3$ containing 0.1, 0.5, 0.7, and 1.0 mol.% Ce per mole of Co, respectively. The catalysts were prepared by a conventional impregnation method. The physical properties of the catalyst before and after the reaction are compared, and based on the results, a PSR mechanism is proposed.

2. Results and Discussion

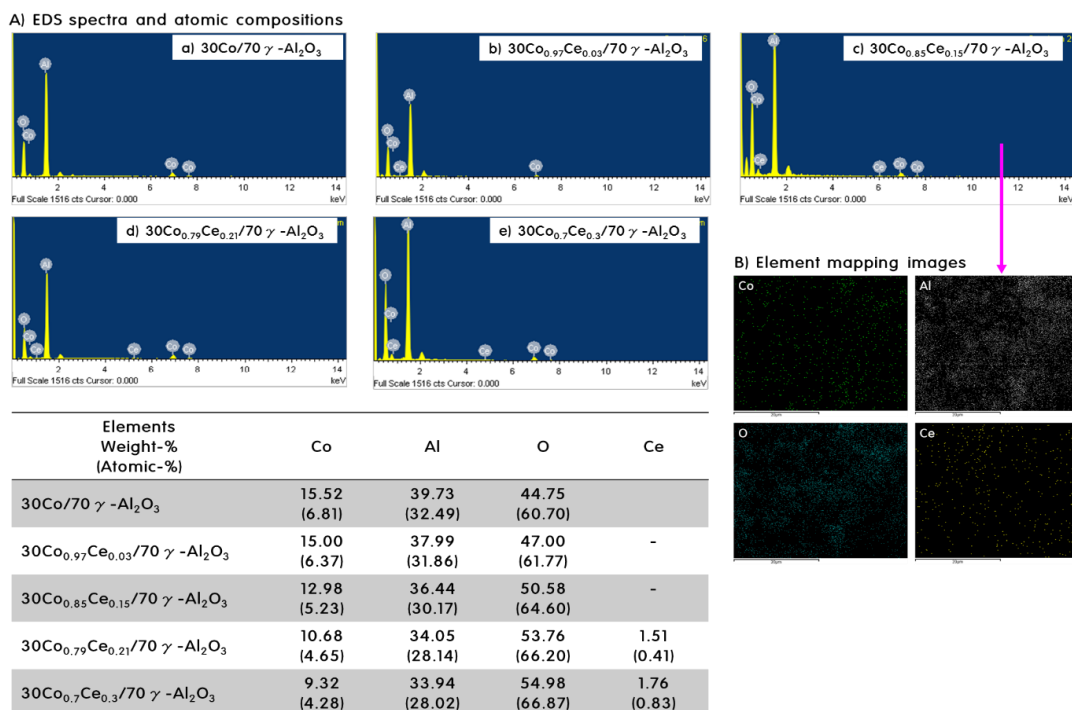### 2.1. Characteristics of $30Co_xCe_y/70\gamma$-Al_2O_3 Catalysts

The crystallinities and phase purities of the as-prepared $30Co_xCe_y/70\gamma$-Al_2O_3 catalysts were determined by XRD analysis, as shown in Figure 1A. The XRD pattern of the pure $30Co/70\gamma$-Al_2O_3 catalyst was assigned to a cubic form of Co_3O_4 in the *Fd-3m* space group [JCPDS card no. 01-073-1701]. The main peaks observed at 2θ = 31.27° (220), 33.85° (311), 44.80° (400), 59.36° (511), and 65.24° (440) were assigned to $CoAl_2O_4$ [JCPDS card no. 00-003-0896]. These results confirm that the Co_3O_4 and $CoAl_2O_4$ phases co-exist in the prepared samples [25]. However, in the case of the $30Co_xCe_y/70\gamma$-Al_2O_3 catalyst, the amount of Ce in the sample was insufficient to yield diffraction peaks corresponding to CeO_2, even though Ce had been added. Only the $30Co_{0.7}Ce_{0.3}/70r$-Al_2O_3 catalyst with the highest amount of Ce showed a weak diffraction peak at 28.57°, corresponding to the (111) crystal face of CeO_2 [JCPDS card no. 00-002-1306]. Interestingly, compared with the diffraction patterns of the $30Co/70\gamma$-Al_2O_3 catalyst, the diffraction peaks of the $30Co_xCe_y/70\gamma$-Al_2O_3 catalysts shifted to higher angles with increasing Ce addition. Thus, according to Bragg's law, the distance (*d*) between the lattice planes was reduced [26]. In addition, the increase in crystal size and lattice strain arise from the differences in the ionic radii of Co and Ce. The TEM images are shown in Figure 1B. The surfaces of the $30Co_xCe_y/70\gamma$-Al_2O_3 catalysts were found to have short rod-like particles of Co and Ce species on the surface of the spherical γ-Al_2O_3 support.

The elemental ratios of the catalysts were examined using EDS/element mapping, and the results are shown in Figure 2A,B. Due to the small amount of Ce (beyond the limit of EDS analysis, which only observed a small part of the surface), the presence of Ce was only confirmed in $30Co_{0.79}Ce_{0.21}/70\gamma$-$Al_2O_3$ and $30Co_{0.70}Ce_{0.30}/70\gamma$-$Al_2O_3$. The amounts of Ce present in these catalysts were about 10% and 20% of the amount of Co, respectively, representing 1/2 and 1/3, respectively, of the amounts of Ce added in the synthesis step. These differences are considered to be due to the limitations of EDS analysis. However, because there was an increase in the proportion of Ce with respect to the amount added, we determined that the catalysts had been successfully formed. Elemental mapping images are shown in Figure 2B and were used to confirm the presence of trace elements contained in the $30Co_{0.85}Ce_{0.15}/70\gamma$-$Al_2O_3$ catalyst. Fortunately, Ce, which did not appear in the EDS spectrum, was found to be evenly dispersed over the catalyst surface. Further, when the intensities of the colored spots corresponding to the respective elements were determined, the intensities of the

spots were found to vary in proportion with the amount of the elements present in the catalyst. Thus, we concluded that the catalysts prepared in this study had been synthesized quantitatively.
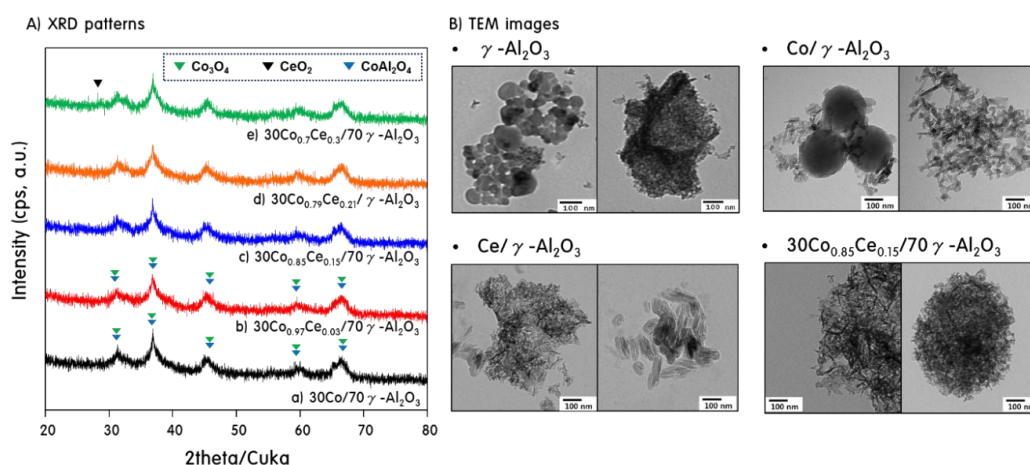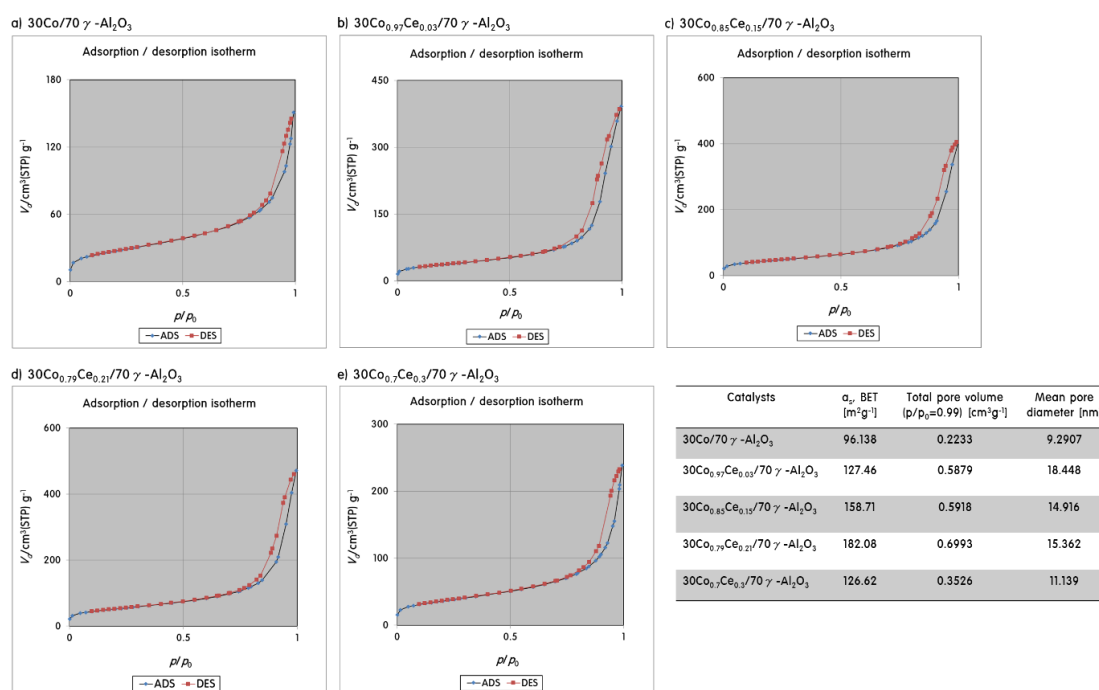

Figure 1. XRD patterns and TEM images of the fresh $30Co_xCe_y/70\gamma$-Al_2O_3 catalysts.

Elements Weight-% (Atomic-%)	Co	Al	O	Ce
$30Co/70\gamma$-Al_2O_3	15.52 (6.81)	39.73 (32.49)	44.75 (60.70)	
$30Co_{0.97}Ce_{0.03}/70\gamma$-$Al_2O_3$	15.00 (6.37)	37.99 (31.86)	47.00 (61.77)	–
$30Co_{0.85}Ce_{0.15}/70\gamma$-$Al_2O_3$	12.98 (5.23)	36.44 (30.17)	50.58 (64.60)	–
$30Co_{0.79}Ce_{0.21}/70\gamma$-$Al_2O_3$	10.68 (4.65)	34.05 (28.14)	53.76 (66.20)	1.51 (0.41)
$30Co_{0.7}Ce_{0.3}/70\gamma$-$Al_2O_3$	9.32 (4.28)	33.94 (28.02)	54.98 (66.87)	1.76 (0.83)

Figure 2. EDS spectra and atomic compositions (**A**) of all catalysts and mapping images for elements (**B**) present in the $30Co_{0.85}Ce_{0.15}/70\gamma$-$Al_2O_3$ catalyst.

Figure 3 shows the N_2 adsorption/desorption isotherm curves obtained at 77 K for the fresh $30Co_xCe_y/70\gamma$-Al_2O_3 catalysts. Using Kelvin's equation, the radii of pores in which capillary condensation occurs can be determined as a function of the relative pressure (P/P_0). The mean pore diameter, D_p, was calculated from $D_p = 4VT/S$, where VT is the total volume of the pores and S is the BET surface area. According to the International Union of Pure and Applied Chemistry classification, the isotherms of all catalysts are type IV. In addition, hysteresis was observed at high relative pressures for all the catalysts, indicating the presence of bulk mesopores formed between the particles. The changes in the mean surface area and pore volume are listed in each figure. The BET specific surface areas of the $30Co_xCe_y/70\gamma$-Al_2O_3 catalysts (127–182 m^2 g^{-1}) are significantly higher than that of the $30Co/70\gamma$-Al_2O_3 catalyst (96 m^2 g^{-1}). In particular, except for

the $30Co_{0.7}Ce_{0.3}/70\gamma$-$Al_2O_3$ catalyst, the BET specific surface area increased as the amount of added Ce increased. In the $30Co_{0.7}Ce_{0.3}/70\gamma$-$Al_2O_3$ catalyst, the specific surface area was slightly reduced because of the strong connections between the large quantity of cerium oxide. In general, the specific surface area of regular particles is strongly related to the particle size, with smaller particles having a greater surface area [27]. Moreover, when the surface area is large, the catalytic active site also increases, and as a result, the catalyst performance tends to increase [28]. The surface area of the catalyst in this study seems to be more affected by the bulk pores formed by sintering particles than their particle size, meaning that there was significant space between particles in the $30Co_xCe_y/70\gamma$-Al_2O_3 catalysts; this might increase the gas adsorption sites for reaction. On the other hand, the total pore volumes and pore diameters in all catalysts showed the same trend with the surface area.

Catalysts	a_s, BET $[m^2g^{-1}]$	Total pore volume $(p/p_0=0.99)$ $[cm^3g^{-1}]$	Mean pore diameter [nm]
$30Co/70\gamma$-Al_2O_3	96.138	0.2233	9.2907
$30Co_{0.97}Ce_{0.03}/70\gamma$-$Al_2O_3$	127.46	0.5879	18.448
$30Co_{0.85}Ce_{0.15}/70\gamma$-$Al_2O_3$	158.71	0.5918	14.916
$30Co_{0.79}Ce_{0.21}/70\gamma$-$Al_2O_3$	182.08	0.6993	15.362
$30Co_{0.7}Ce_{0.3}/70\gamma$-$Al_2O_3$	126.62	0.3526	11.139

Figure 3. N_2 adsorption/desorption isotherm curves at 77 K for the fresh $30Co_xCe_y/70\gamma$-Al_2O_3 catalysts.

Many previous studies [29,30] have confirmed that the activities of catalysts containing reduced metals rather than metal oxides are better for hydrocarbon reforming. Therefore, reduced catalysts were used in this study, and H_2-TPR measurements of all catalysts were performed to determine the appropriate reduction temperature. Figure 4A shows the H_2-TPR profiles of the $30Co_xCe_y/70\gamma$-Al_2O_3 catalysts, where the peak area corresponds to the hydrogen uptake and the peak position corresponds to the reduction temperature of the catalyst species. In general, the reduction peak for pure Co_3O_4 to CoO is observed at about 250 °C, whereas the peak for CoO to Co metal occurs at about 400 °C [31]. From the XRD pattern shown in Figure 1, we confirmed that all the catalysts contained Co_3O_4 and $CoAl_2O_4$. Finally, the TPR profile for $30Co/70\gamma$-Al_2O_3 shows a large peak at 850 °C, corresponding to the reduction of the stoichiometric cobalt aluminate species (spinel $CoAl_2O_4$) [32]. Two distinct peaks centered at 420 and 500 °C were observed, which are attributed to the two-step reduction of Co_3O_4 to CoO and then to Co, respectively, which interacts with the Al_2O_3 support [33]. However, in the catalysts substituted with Ce, Co partially escapes from the skeleton and is present outside the lattice as Co_3O_4. The reduction peak for this, i.e., the peak corresponding to the reduction of Co_3O_4 to CoO, was observed at about 200 °C. Furthermore, in the catalysts containing Ce, the reduction of Co_3O_4 and CoO occurs at lower temperatures, about 400 °C. In particular, the reduction of Co ions in $CoAl_2O_4$, which usually occurs at high temperatures, also shifted to a low temperature of about 700–800 °C. Thus, the addition of Ce into the framework lattice facilitates the removal of lattice oxygen, and thus,

more Co is reduced. This means that the oxygen in the Co-O-Ce lattice is more easily removed than in the Co-O-Co lattice. On the other hand, in the $30Co_{0.7}Ce_{0.3}/70r\text{-}Al_2O_3$ catalyst, which has the highest Ce substitution, a peak was observed in which Ce^{4+} was reduced to Ce^{3+} at about 550 °C (strictly speaking, this corresponds to the oxygen vacancy of cerium oxide). Finally, as the amount of added Ce increased, the peaks shifted to low temperature, suggesting that the reduction is affected by the synergistic effect of Co and Ce. Possibly, the increase in the strain induced by the addition of Ce improves the reduction of the catalyst by reducing the strength of the metal–oxygen bond [34]. Based on the TPR profiles, all the catalysts were pretreated with hydrogen at 700 °C before PSR, and the XRD patterns of the catalysts after reduction are shown in Figure 4B. Metallic Co was observed in the XRD patterns of the $30Co_xCe_y/70\gamma\text{-}Al_2O_3$ catalysts. However, the amount of metallic Co decreased with increasing Ce substitution, and many peaks corresponding to Co_3O_4 and $CoAl_2O_4$ remained. In addition, diffraction peaks corresponding to metallic Ce (reduced from cerium oxide) were not observed in any catalyst, but the peak at 32°, which arises from Ce_2O_3, was stronger only in the most substituted $30Co_{0.7}Ce_{0.3}/70r\text{-}Al_2O_3$ catalyst.
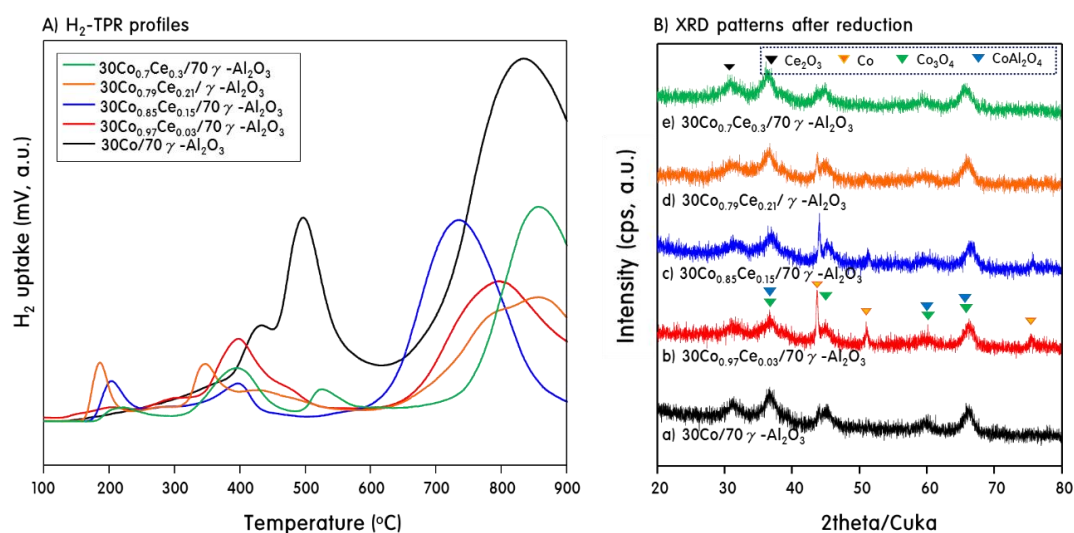
Figure 4. H_2-TPR curves of the fresh $30Co_xCe_y/70\gamma\text{-}Al_2O_3$ catalysts and XRD patterns of the reduced $30Co_xCe_y/70\gamma\text{-}Al_2O_3$ catalysts.

2.2. Gas Adsorption Ability of $30Co_xCe_y/70\gamma\text{-}Al_2O_3$ Catalysts

In general, the reactivity of a catalyst is closely related to the reactant adsorption capacity. Therefore, to investigate the adsorption capacity for C_3H_8 (the feed gas) and CO (the intermediate gas), C_3H_8-, and CO-TPD were performed, and the results are shown in Figure 5A,B, respectively. Chemisorption is the process by which adsorbed species on the catalyst surface are combined and the product is desorbed from the surface; usually, a catalyst with a high gas adsorption capacity is also highly active [35]. In the case of the $30Co/70\gamma\text{-}Al_2O_3$ catalyst, propane desorption peaks were observed near 420 and 800 °C. On the other hand, most Ce-containing catalysts showed low desorption peaks at low temperatures and large desorption peaks at high temperatures. In particular, compared with the $30Co/70\gamma\text{-}Al_2O_3$ catalyst, the high-temperature (800 °C) desorption peak shifted to a lower temperature (near 700 °C), and the quantity desorbed also remarkably increased. These results suggest that the addition of Ce improves the interaction between propane gas and the catalyst and more propane is adsorbed during the propane steam reforming reaction at high temperatures. On the other hand, the results for CO-TPD are shown in Figure 5B. There are three losses at 100 (even though very small), 200, and 400 °C on $30Co/70\gamma\text{-}Al_2O_3$. The CO desorption usually occurs in three parts: The loss curve corresponding to the desorption of CO molecules physically adsorbed on the catalyst surface occurs at about 100–150 °C, whereas the desorption curve for CO molecules chemically adsorbed on

the catalyst surface is observed at about 200–600 °C. Finally, CO gas strongly adsorbs to the lattice, and a curve corresponding to the desorption of CO_2 bound to the lattice oxygen is observed at about 700–900 °C [36]. For the $30Co/70\gamma$-Al_2O_3 catalyst, only the desorption of CO molecules adsorbed physically or chemically on the surface of the cobalt oxide was observed. However, when Ce was added, the CO desorption shifted to higher temperatures. Generally, higher desorption temperatures indicate stronger interactions between CO and the catalyst. Furthermore, the CO_2 desorption curve was observed at about 850 °C for the $30Co_xCe_y/70\gamma$-Al_2O_3 catalysts. Other studies have also reported CO adsorption on CeO_2 ($2CeO_2 + CO \rightarrow Ce_2O_3 + CO_2$) [37]. This result suggests that the Ce-substituted catalysts can easily release oxygen from the lattice, and ultimately, form oxygen vacancies within the lattice. Additionally, the adsorption of CO on $30Co_xCe_y/70\gamma$-Al_2O_3 with increasing Ce content also increased compared to that of $30Co/70\gamma$-Al_2O_3. This means that the addition of Ce favors the adsorption of CO, and thus, promotes the PSR and WGS reactions.
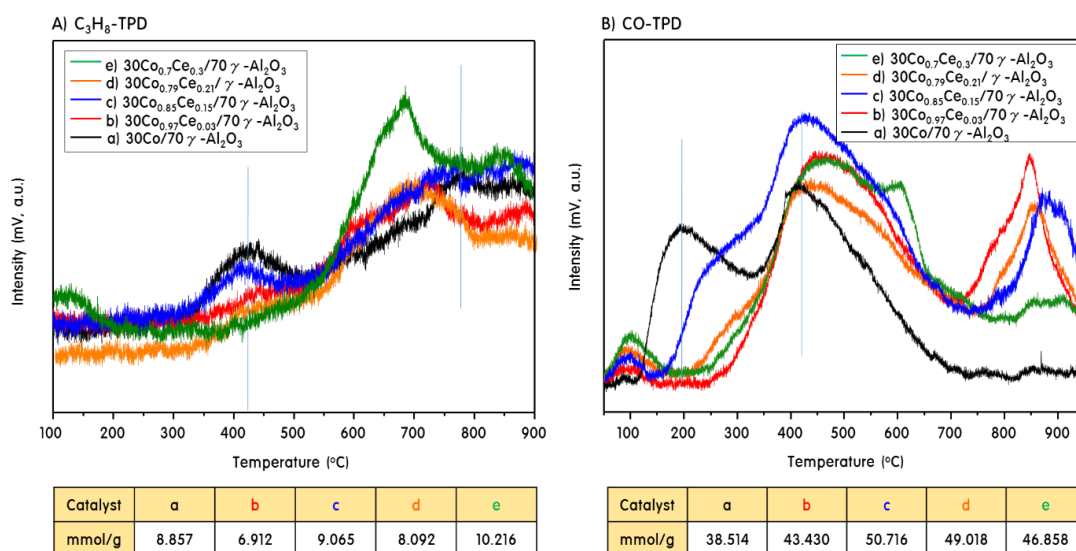

Catalyst	a	b	c	d	e
mmol/g	8.857	6.912	9.065	8.092	10.216

Catalyst	a	b	c	d	e
mmol/g	38.514	43.430	50.716	49.018	46.858

Figure 5. C_3H_8- and CO-TPD curves for the fresh $30Co_xCe_y/70\gamma$-Al_2O_3 catalysts.

In a hydrocarbon steam reforming reaction, water vapor (H_2O) is another major feed gas and is involved in the WGS reaction. The water gas shift reaction is [38] $CO + H_2O \rightarrow CO_2 + H_2$, ΔH = −41.1 kJ/mol. It is possible to increase the thermal stability of the catalyst by converting CO, which causes the deterioration of the catalyst, to CO_2. Therefore, H_2O desorption experiments were performed on both catalysts, $30Co/70\gamma$-Al_2O_3 and $30Co_{0.85}Ce_{0.15}/70\gamma$-$Al_2O_3$, using the TGA equipment to calculate the activation energy for water adsorption on the catalysts. Figure 6A shows the results of H_2O desorption experiments, and the plot of $\ln(\psi/T_m^2)$ versus $1/T_m$ using the Ozawa equation [39] is shown in Figure 6B. The water desorption activation energies can be calculated from the slope of the plot. The activation energies of desorption for the $30Co/70\gamma$-Al_2O_3 and $30Co_{0.85}Ce_{0.15}/70\gamma$-$Al_2O_3$ catalysts were calculated to be 189.73 and 266.96 kJ/mol, respectively. Therefore, it is expected that the steam added to the feed gas of the PSR reaction will be adsorbed better on the surface of Ce than that of Co. In particular, Yan Li et al. [40] reported that Ce addition not only increases the dispersion of the active metals, but also accelerates the adsorption and activation of steam, as shown by the following Equation [41]: $H_2O + Ce_2O_3 \rightarrow 2CeO_2 + H_2$. Therefore, based on the overall gas-TGA results, we suggested that Co would be activated, perhaps synergistically with Ce. Therefore, the hydrocarbon reforming reaction occurs mainly on Co sites during the PSR reaction, and the WGS reaction can be promoted, whereas water adsorption occurs mainly on Ce.
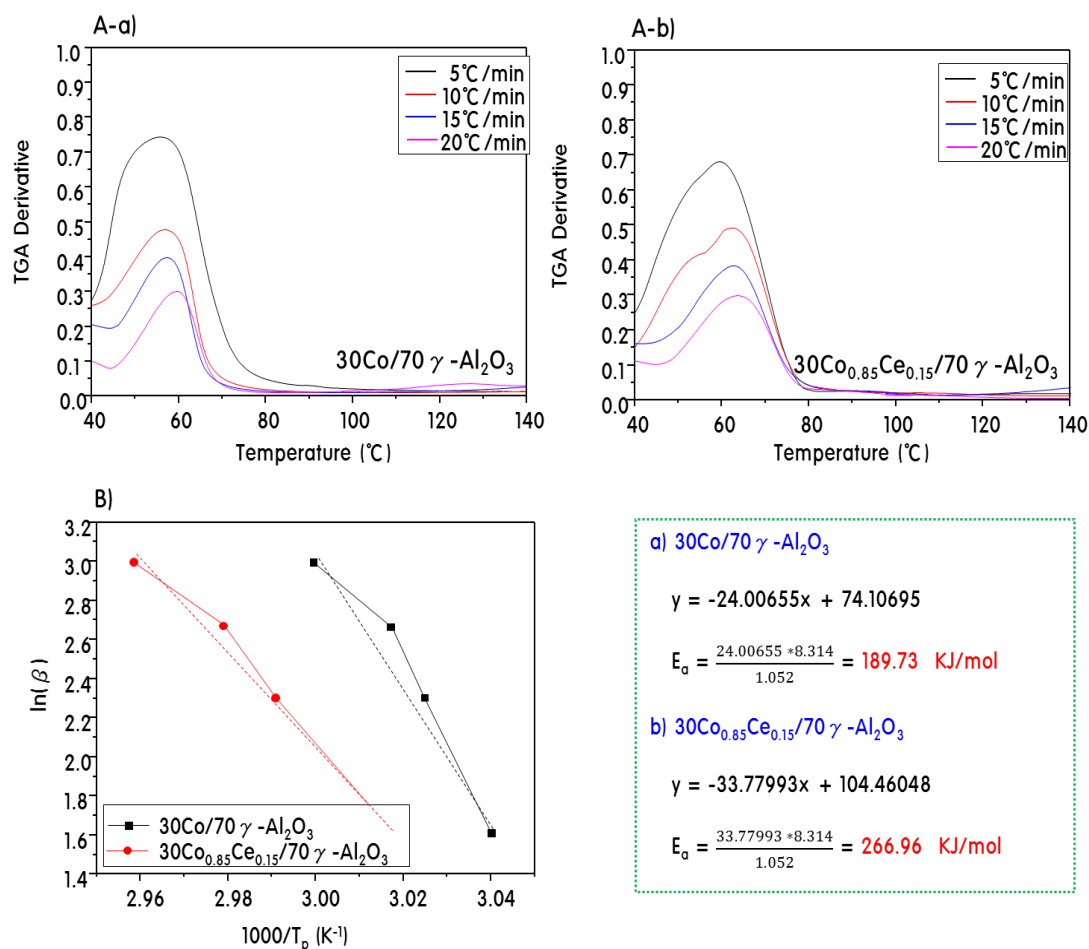
Figure 6. TGA curves (**A**) for H_2O-desorption and the activation energies (**B**) calculated from Ozawa plots for the $30Co/70\gamma$-Al_2O_3 and $30Co_{.85}Ce_{0.15}/70\gamma$-$Al_2O_3$ catalysts.
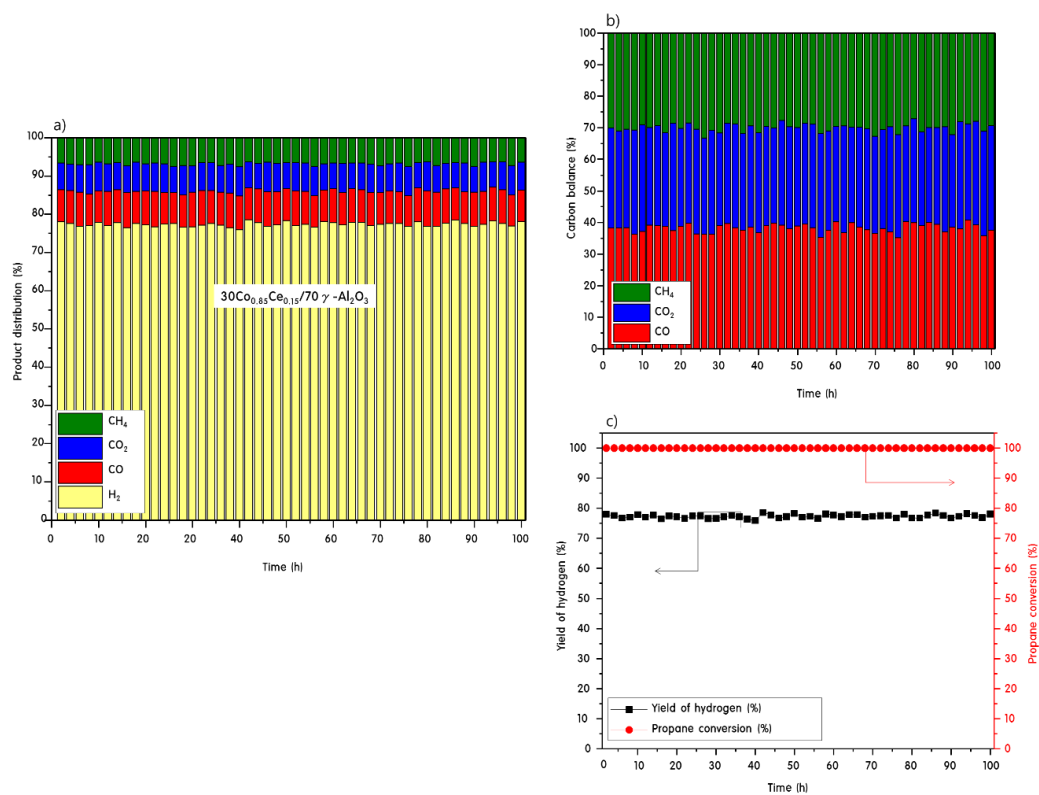
2.3. Propane Steam Reforming Reaction over $30Co_xCe_y/70\gamma$-Al_2O_3 Catalysts

Figure 7 shows the product distributions of all catalysts during the PSR reaction at 700 °C for 10 h. The $30Co_{0.85}Ce_{0.15}/70\gamma$-$Al_2O_3$ and $30Co_{0.79}Ce_{0.21}/70\gamma$-$Al_2O_3$ catalysts showed 100% propane conversion, whereas $30Co/70\gamma$-Al_2O_3, $30Co_{0.97}Ce_{0.03}/70\gamma$-$Al_2O_3$, and $30Co_{0.7}Ce_{0.3}/70\gamma$-$Al_2O_3$ showed a propane conversion of over 90%. Here, the values for all PSR experiments are the average of the results of three runs. The products detected by GC were H_2, CO, CH_4, and CO_2, and the product distribution ratios were different for each catalyst. During the PSR of the $30Co/70\gamma$-Al_2O_3 catalyst, H_2, CO, and CH_4 were identified as major products and little CO_2 was observed. On the other hand, the catalysts with added Ce exhibited increased propane conversion and absolute hydrogen production during the PSR, and CO_2 production was greatly increased with a decreasing amount of CO produced. This can be interpreted as a result of the accelerated WGS reaction induced by Ce. Here, ceria might easily form oxygen vacancies and supply oxygen to CO, as shown by the following equation: $2CeO_2 \leftrightarrow Ce_2O_3 + 0.5O_2$. Thus, the $30Co_{0.85}Ce_{0.15}/70\gamma$-$Al_2O_3$ catalyst is the optimal catalyst when considering propane conversion and the product distribution.

For the best catalyst, $30Co_{0.85}Ce_{0.15}/70\gamma$-$Al_2O_3$, the longevity was measured by increasing the reaction time at 700 °C to 100 h. These measurements allowed us to examine the lifetime of the catalyst. The results are shown in Figure 8. The 100% propane conversion and 78% hydrogen yield did not show any decline after 100 h. Furthermore, the amount of carbon compounds produced as intermediates or as products were constant for 100 h. This result indicates that the oxygen transport of cerium oxide in the $30Co_{0.85}Ce_{0.15}/70\gamma$-$Al_2O_3$ catalyst prevents the Co from being completely reduced, and consequently, the deactivation of Co can be suppressed and the lifetime of the catalyst increased.
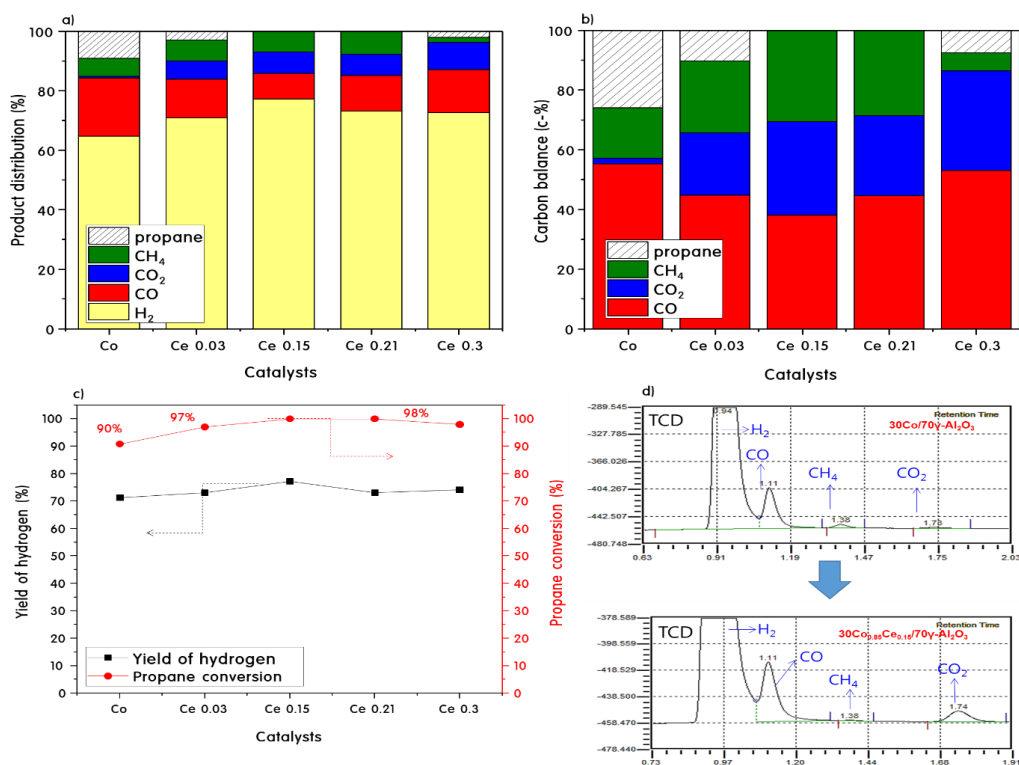
Figure 7. Product distributions (**a**,**b**) and hydrogen yield and propane conversion (**c**) during propane steam reforming reaction at 700 °C after 10 h and GC signals (**d**).

Figure 8. Product distributions (**a**,**b**) and hydrogen yield and propane conversion (**c**) for the $30Co_{0.85}Ce_{0.15}/70\gamma$-$Al_2O_3$ catalyst during the PSR reaction at 700 °C over 100 h.

2.4. Characteristics of $30Co_xCe_y/70\gamma$-Al_2O_3 Catalysts after Propane Steam Reforming

Figure 9 shows the TGA (and TPO) curves for coke combustion, as well as TEM images of the catalysts after PSR. We used the TEM images to determine the amount and shape of the carbon deposited on the catalyst after PSR. The TPO curve is also shown in this figure. Generally, the TPO curves are separated into three peaks at 100–200, 350, and 550 °C, respectively. Aside from the water desorption curve below 200 °C, the positions of combustion peaks on monometallic sites and bimetallic sites are related to the interaction between the metal and deposited carbon, as well as the shape of the deposited carbon particles. Usually, the coke deposited on monometallic sites burns at higher temperatures than bimetallic sites [42]. However, in this study, we could not make this generalization, i.e., the coke deposited on the Co monometallic sites on the Al_2O_3 support burnt at a low temperature of around 450 °C, and the peak at 580 °C was associated with a coke fraction deposited on the Co–Ce bimetallic sites. In this study, the burning of coke at higher temperatures in the Ce-substituted catalyst indicates that the shape of the formed coke particles is different. Thus, the PSR pathways on the Co metal and cobalt oxides were different, the resulting intermediates were different, and consequently, the shapes of the deposited coke particles were also different. Coke burned at a low temperature is probably an amorphous encapsulating carbon, whereas the burned coke at a high temperature probably has a crystalline whisker carbon structure such as carbon nanotubes. From the TGA analysis, the carbon deposits on the $30Co/70\gamma$-Al_2O_3, $30Co_{0.97}Ce_{0.03}/70\gamma$-$Al_2O_3$, $30Co_{0.85}Ce_{0.15}/70\gamma$-$Al_2O_3$, $30Co_{0.79}Ce_{0.21}/70\gamma$-$Al_2O_3$, and $30Co_{0.7}Ce_{0.3}/70\gamma$-$Al_2O_3$ catalysts were 2.98%, 0.34%, 1.84%, 4.13%, and 5.42%, respectively. The amount of deposited coke tended to increase with increasing Ce substitution. The reason that the correlation between the amount of Ce and the amount of coke shows an opposing trend, that is, propane conversion in all the catalysts did not reach 100%. This seems to be attributed to the fact that, as the amount of Ce increased, the amount of Co participating in the substantial reforming reaction decreased, resulting in a decrease in the amount of CH_4 combustion, and consequently, an increase in the carbon deposition probability. In other words, the carbon compounds, produced as intermediates, strongly interacted with the surface of the catalysts with greater Ce substitution; thus, they could not escape from the catalyst surface and accumulated. However, based on these results, we found that the addition of 15% Ce (with respect to that of Co) can suppress coke formation, as well as catalyst deactivation. To confirm this result, TEM images were obtained to determine the shape of the deposited carbon particles. The amount of carbon deposited was too small to observe particular carbon shapes such as carbon nanotubes (CNTs) or fullerenes. Nonetheless, the catalyst without Ce clearly exhibited agglomeration between metals, and the particles measuring 100 nm in diameter, before reaction, grew to micrometer size. These enormous particles inactivate the catalytic sites and the deposited carbon could not be easily burned away; thus, carbon is continuously deposited, resulting in coke formation. On the other hand, in the catalysts with Ce substitution, the needle-shaped particles before reaction did not increase in size after the reaction, but became highly dispersed. Possibly, the introduction of Ce_xO_y suppressed sintering between Co metal particles (actually CoO). This means that even if carbon is deposited on the surface of the catalyst, it could be easily burned away on the Ce_xO_y to inhibit coke formation, resulting in continuous catalyst activity.

Figure 10 shows the Co_{2p}, Ce_{3d}, Al_{2p}, and O_{1s} XPS spectra of two representative catalysts, $30Co/70\gamma$-Al_2O_3 and $30Co_{0.85}Ce_{0.15}/70\gamma$-$Al_2O_3$, before and after PSR. The Co_{2p} spectra contain peaks corresponding to Co^{2+} (783.52 eV) and $Co^{2.5+}$ (781.36 eV) for both catalysts before reaction [43]. However, after reaction, the peaks moved towards lower binding energies, which means the formation of reduced Co species. However, the migration was not significant for $30Co_{0.85}Ce_{0.15}/70\gamma$-$Al_2O_3$. This is because Co can continue to be supplied with oxygen by the cerium oxide [44], and it would not have been perfectly reduced into Co metal after the PSR reaction. Eventually, the oxygen supply of Ce prevents sintering between the reduced Co metal particles, which slows the deterioration of the catalyst. In the O_{1s} spectrum, various types of oxygen species were observed before PSR, but they converged to the oxygen present in the lattice after PSR, moving toward a small binding energy at 531.06 eV [45]. This means that the oxidation state of the metals present after the reaction has

become simple and significant, oxygen has been lost from the lattice. This phenomenon was more significant in the catalysts containing Ce. The Al_{2p} spectrum of the catalysts before PSR contains peaks corresponding to Al-O and Al-O-H at 74.2 and 76.8 eV, respectively [44]. After the reaction, the only Al peak in the lattice was observed at 74.1 eV. This result suggests that Al also participates in the PSR reaction to some degree, perhaps acting as an oxygen transfer medium, although the effect of Al weaker than that of cerium oxide. Based on the $Ce_{3d5/2}$ peak at 885.50 eV [46], we confirmed that the Ce was present as an oxide before and after the reaction, whereas it was present as Ce^{4+} before the reaction. After reaction, the peak moved to a lower binding energy as a result of reduction (probably to Ce^{3+}). Finally, the C_{1s} spectrum is presented for analysis of the carbon content deposited after the reaction. After the reaction, two peaks corresponding to C=O and C=C were observed at 284.90 and 284.27 eV [47]. The amount of accumulated carbon was greater on the $30Co/70\gamma$-Al_2O_3 catalyst than that on the $30Co_{0.85}Ce_{0.15}/70\gamma$-$Al_2O_3$ catalyst. Otherwise, the peak positions for C=O and C=C shifted to the higher binding energies of 288.25 and 284.90 eV on the $30Co_{0.85}Ce_{0.15}/70\gamma$-$Al_2O_3$ catalyst. As already mentioned from the TPO results, C=O corresponds to amorphous carbon and C=C is considered to correspond to a crystalline carbon such as CNT. This result means that the mechanisms on two catalysts were different depending on Ce addition.

Based on the catalytic performance for the PSR and physicochemical characteristics, Scheme 1 presents a proposed PSR mechanism for the $30Co_{0.85}Ce_{0.15}/70\gamma$-$Al_2O_3$ catalyst. During reforming, the Co or Co_xO_y components play important roles in the dehydrogenation and thermal cracking of propane gas, transforming the propane gases to C_2H_4 and CH_4 as an intermediate and then acetaldehyde (CH_3CHO), generated by ethylene oxidation over bimetallic CoCeO [48,49]. The acetaldehyde was thermally and catalytically cracked to CH_4 and CO. The CH_4 and CO obtained were accompanied by other reactions, such as the CH_4-steam reforming reaction and CO-WGS reaction. Based on CO- and H_2O-TPD experiments, water molecules were well adsorbed on cerium oxide components and CO molecules were well adsorbed on the bimetallic CoCeO components. Finally, the oxygen vacancies were filled because of the interaction with water vapor and oxygen donated sites in cerium oxide. Meanwhile, the CO-water gas shift reaction took place predominantly on CoCeO bimetallic oxide. Based on the excellent oxygen delivery properties of Ce, the vapor (H_2O) participates in the WGS reaction on the cerium oxide surface produce H_2 and CO_2. In conclusion, cerium oxide, as a promoter, helps to produce a high hydrogen yield in the PSR reaction when using the $30Co_{0.85}Ce_{0.15}/70\gamma$-$Al_2O_3$ catalyst.
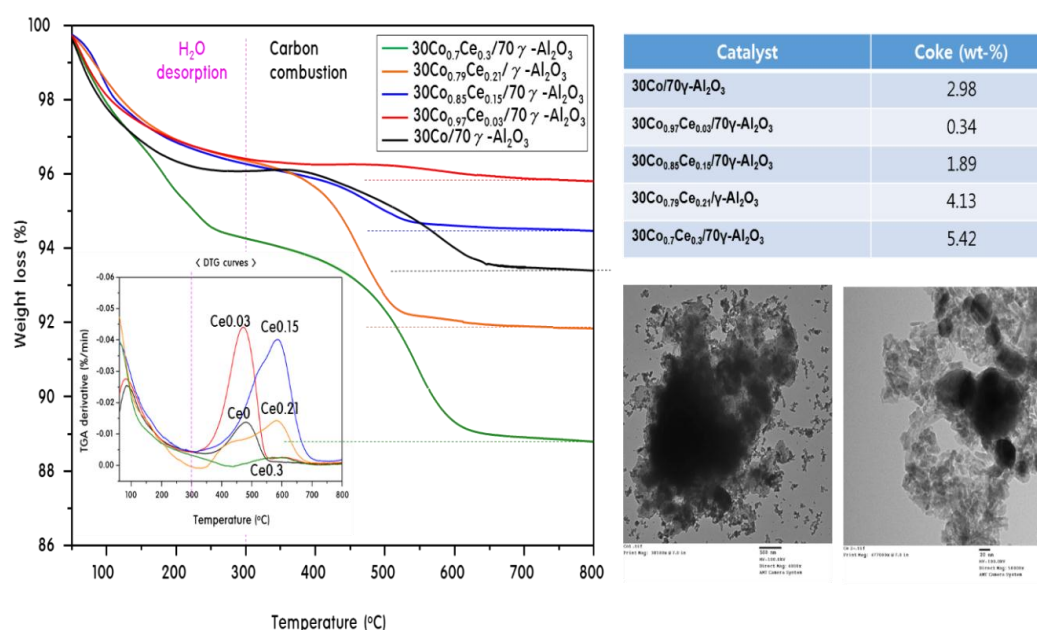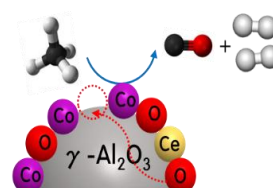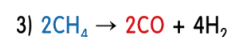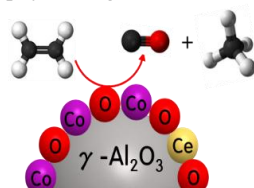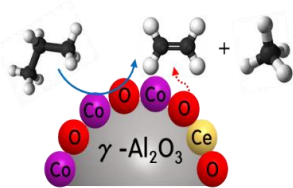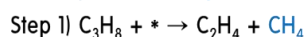

Figure 9. TGA and TPO curves for coke combustion and TEM images of the used $30Co_xCe_y/70\gamma$-Al_2O_3 catalysts after PSR.
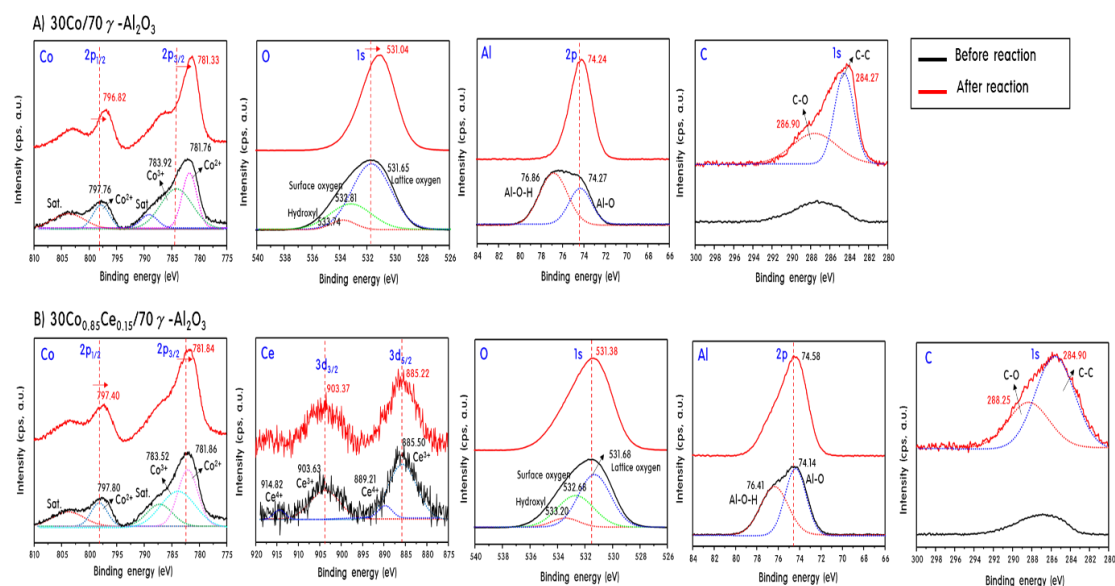
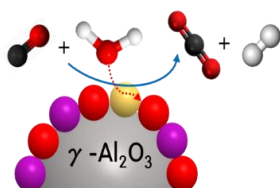**Figure 10.** XPS of the two representative catalysts, 30Co/70γ-Al$_2$O$_3$ (**A**) and 30Co$_{.85}$Ce$_{0.15}$/70γ-Al$_2$O$_3$ (**B**), before and after PSR.

⟨Adsorption-Cracking-Steam reforming⟩

Step 1) C_3H_8 + * → C_2H_4 + CH_4 2) C_2H_4 → (CH_3CHO) → CO + CH_4 3) $2CH_4$ → 2CO + $4H_2$

⟨Water gas shift reaction⟩

Step 1) 3CO + $3H_2O$ → $3CO_2$ + $3H_2$

Scheme 1. Expected PSR mechanism on the 30Co$_{0.85}$Ce$_{0.15}$/70γ-Al$_2$O$_3$ catalyst.

3. Experimantal

3.1. Preparation of 30Co$_x$Ce$_y$/70 γ-Al$_2$O$_3$ Catalysts

The 30Co$_x$Ce$_y$/70γ-Al$_2$O$_3$ catalysts were prepared using a conventional impregnation method at pH 3.0, and the obtained catalysts are denoted 30Co$_x$Ce$_y$/70γ-Al$_2$O$_3$ (x = 1, 0.97, 0.85, 0.79, and 0.70 and y = 0, 0.03, 0.15, 0.21, and 0.30; thus, the Ce contents were 0.1, 0.5, 0.7, and 1.0 mol.% per mole of Co) based on the added elements and ratios. Cobalt chloride (CoCl$_2$, Daejung Chemicals & Metals Co., Ltd., Siheung, Korea) and cerium chloride (CeCl$_4$, Daejung Chemicals & Metals Co., Ltd., Siheung, Korea) were used as metal precursors for Co and Ce. First, the appropriate amounts of CoCl$_2$ and cerium chloride were dissolved in a 500-mL beaker containing ethanol solvent with continuous stirring. The pH values of the solutions were adjusted to 3.0 with acetic acid so that the two metals were completely dissolved, and constant stirring of the solution was carried out for about 1 h. Subsequently, 10.0 g of γ-Al$_2$O$_3$ powder was added to the above solution, which

was stirred again for 12 h at room temperature and then evaporated at 80 °C for 2 h to remove the solvents and impurities. The obtained powders were calcined in air at 700 °C for 5 h to crystallize; finally, the five powdered catalysts were obtained: $30Co/70\gamma\text{-}Al_2O_3$, $30Co_{0.97}Ce_{0.03}/70\gamma\text{-}Al_2O_3$, $30Co_{0.85}Ce_{0.15}/70\gamma\text{-}Al_2O_3$, $30Co_{0.79}Ce_{0.21}/70\gamma\text{-}Al_2O_3$, and $30Co_{0.70}Ce_{0.30}/70\gamma\text{-}Al_2O_3$. These catalysts were subjected to prehydrogen reduction at 700 °C for 2 h before use for PSR.

3.2. Characterization

X-ray diffraction (XRD, MPD, PANalytical, Almelo, The Nederland) measurements using nickel-filtered Cu $K\alpha$ radiation (40 kV, 30 mA) were carried out to identify the structure and crystallinity of the synthesized $30Co_xCe_y/70\gamma\text{-}Al_2O_3$ catalysts. The catalyst particle shapes were determined by high-resolution transmission electron microscopy (TEM, H-7600, Hitachi, Tokyo, Japan) operated at 120 kV. X-ray photoelectron spectroscopy (XPS, AXIS Nova, Kratos Inc., San Diego, CA, USA) measurements for Co_{2p}, Ce_{3d}, Al_{2p}, O_{1s}, and C_{1s} were performed using a non-monochromatic Al $K\alpha$ (1486.6 eV) X-ray source. The elemental compositions of the catalysts were determined using an energy-dispersive X-ray spectroscope (EDS, EX-250, Horiba, Kyoto, Japan) operated at 15 kV. The Brunauer–Emmett–Teller (BET) surface areas of the catalysts were obtained from liquid nitrogen adsorption/desorption isotherm curves measured using a Belsorp II instrument (Belsorp II Mini, Toyonaka, Japan).

H_2-temperature programmed reduction (TPR), and CO- and C_3H_8-TPD (temperature programmed desorption) were conducted with a BELCAT (Bel Japan Inc., Toyonaka, Japan). 0.10 g of the calcined sample was charged into the quartz tube and flushed with high-purity argon gas at 300 °C for 1 h, followed by cooling to room temperature. The catalyst for TPR was charged into the quartz tube and reduced in 5 vol% H_2/Ar (ca. 30 mL min^{-1}) from 50 to 900 °C. Wherein CO and C_3H_8 gases for TPD were introduced as adsorption gases (ca. 30 mL min^{-1}) at 50 °C for 1 h. After adsorption, the system was purged with argon gas for 30 min to remove any weakly adsorbed species. The tests were initiated by heating to 900 °C at a rate of 10 °C min^{-1}. The resulting profile was monitored using a thermal conductivity detector (TCD) and mass analyzer [Q-mass].

Thermogravimetric analysis (TGA) for coke combustion (TPO, temperature programmed oxidation) after reaction was conducted using a thermos differential and gravimetric analyzer (Shinco, Daejeon, Korea). The samples weighed 7.0–10.0 mg. The TGA data based on weight loss were collected in the 50–800 °C temperature range at a rate of 10 °C min^{-1} in air-flow (ca. 25 mL min^{-1}).

The activation energies for water desorption from the catalysts were also determined using the thermogravimetric analysis apparatus. The data were collected in the range of 40–500 °C at rates of 5, 10, and 15 °C min^{-1} N_2 flow (ca. 25 mL min^{-1}). Before the tests, the catalysts were dried in a drying oven at 200 °C for 2 h to remove water molecules attached to the surface. After that, the samples were immediately placed in a desiccator containing a saturated solution of $(NH_4)_2SO_4$ and stored for 24 h to adsorb any water.

A fixed bed-type reactor was already designed in the previous study for the PSR [21]. The catalytic activities of the $30Co_xCe_y/70\gamma\text{-}Al_2O_3$ catalysts were measured at 700 °C for 10 h at a steam-to-propane ratio of 1:6 (mol.%) with a gas hourly space velocity (GHSV) of 6000 h^{-1}. The catalyst (1.0 g) was pelletized to a 20–24 mesh, packed in the fixed-bed quartz reactor, and then mounted vertically inside the furnace. In this study, the amount of steam was adjusted by regulating the temperature according to the partial pressure law. The reaction products during PSR were measured by an on-line gas chromatograph (GC, DS7200, Donam Company, Gwangju, Korea) equipped with a thermal conductivity detector (TCD) and flame-ionizing detector (FID). H_2, CO, CO_2, CH_3CHO, and CH_3COOH were detected with the TCD, whereas CH_4, C_2H_4, C_2H_6, and C_3H_8, and the other products were detected with the FID. The following GC conditions were used: Carboxen-1000 column (Bruker, Billerica, MA, USA); injection temperature, 423 K; initial column temperature, 423 K; final

temperature, 473 K; and detector temperatures, 423 K (TCD) and 573 K (FID). The C_3H_8 conversion, H_2 yield, and C_i (CH_4, CO_2, or CO) selectivity are defined as follows:

$$C_3H_8 \text{ conversion (\%)} = ([C_3H_8]_{in} - [C_3H_8]_{out})/[C_3H_8]_{in} \times 100 \tag{3}$$

$$\text{Hydrogen yield (\%)} = [H_2]_{out}/([H_2]_{in} \text{ in } C_3H_8 + [H_2]_{in} \text{ in } H_2O) \times 100 \tag{4}$$

$$C_i \text{ selectivity (\%)} = [CO, CO_2, \text{ or } CH_4]_{out}/[CO_2 + CO + CH_4]_{out} \times 100 \tag{5}$$

4. Conclusions

The purpose of this study was to improve the catalytic stability of the $30Co/70\gamma\text{-}Al_2O_3$ catalyst and to promote hydrogen production by introducing Ce, which has an excellent oxygen transfer capacity. The catalytic performances of the $30Co_xCe_y/70\gamma\text{-}Al_2O_3$ catalysts were evaluated for the PSR reaction at 700 °C for 10 h. The $30Co_{0.85}Ce_{0.15}/70\gamma\text{-}Al_2O_3$ catalyst showed 100% propane conversion, about 75% H_2 selectivity, and the least carbon deposition after PSR. In particular, because the addition of Ce accelerated the WGS reaction, CO, which causes catalyst poisoning, was converted to CO_2. Considering the gas adsorption capacity, propane conversion, and carbon deposition after reaction, the $30Co_{0.85}Ce_{0.15}/70\gamma\text{-}Al_2O_3$ catalyst is the optimal Ce substitution ratio. Finally, the synergistic effect of Co and Ce in the catalyst for the PSR allowed hydrogen gas to be produced stably without catalyst deactivation after 100 h.

Author Contributions: Conceptualization, J.Y.D., M.K.; Methodology, Formal Analysis, J.Y.D.; Writing-Review & Editing, M.K., R.K.C.; Formal Analysis, N.S. and J.K.; Investigation, N.-K.P; Funding Acquisition, D.L., M.W.S.; Project Administration, H.-J.R., J.H.C.; Supervision, M.K.

Conflicts of Interest: The authors declare no conflict of interest

References

1. Dodds, P.E.; Staffell, I.; Hawkes, A.D.; Grunewald, P.; McDowall, W.; Ekins, P. Hydrogen and fuel cell technologies for heating: A review. *Int. J. Hydrogen. Energy* **2011**, *40*, 2065–2083. [CrossRef]
2. Amin, A.M.; Croiset, E.; Epling, W. Review of methane catalytic cracking for hydrogen production. *Int. J. Hydrogen. Energy* **2011**, *36*, 2904–2935. [CrossRef]
3. Enger, B.C.; Lodeng, R.; Holmen, A. A review of catalytic partial oxidation of methane to synthesis gas with emphasis on reaction mechanisms over transition metal catalysts. *Appl. Catal. A* **2008**, *346*, 1–27. [CrossRef]
4. Wang, S.; Lu, G.Q.; Millar, G.J. Carbon Dioxide Reforming of Methane to Produce Synthesis Gas over Metal-Supported Catalysts: State of the Art. *Energy Fuels.* **1996**, *10*, 896–904. [CrossRef]
5. Rostrup-Nielsen, J. Steam reforming of hydrocarbons. A historical perspective. *Stud. Surf. Sci. Catal.* **2004**, *147*, 121–126.
6. Granger, P.; Parvulescu, V.; Kaliaguine, S.; Prellier, W. *Perovskites and Related Mixed Oxides: Concepts and Applications, Band 1*; John Wiley & Sons: New York, NY, USA, 2015; 1056p.
7. Harshini, D.; Yoon, C.Y.; Han, J.H.; Yoon, S.P.; Nam, S.W.; Lim, T.H. Catalytic steam reforming of propane over $Ni/LaAlO_3$ catalysts: influence of preparation methods and OSC on activity and stability. *Catal. Lett.* **2012**, *142*, 205–212. [CrossRef]
8. Sohn, H.; Ozkan, U.S. Cobalt-Based Catalysts for Ethanol Steam Reforming: An Overview. *Energy Fuels* **2016**, *30*, 5309–5322. [CrossRef]
9. Wu, H.; Parola, V.L.; Pantaleo, G.; Puleo, F.; Venezia, A.M.; Liotta, L.F. Ni-Based Catalysts for Low Temperature Methane Steam Reforming: Recent Results on Ni-Au and Comparison with Other Bi-Metallic Systems. *Catalysts* **2013**, *3*, 563–583. [CrossRef]
10. Jakobsen, J.G.; Jakbensen, M.; Chorkendorff, I.; Sehested, J. Methane Steam Reforming Kinetics for a Rhodium-Based Catalyst. *Catal. Lett.* **2010**, *140*, 90–97. [CrossRef]

11. Zhang, X.; Gong, Y.; Yu, G.; Xie, Y. Oxygen species on NiO/Al$_2$O$_3$ and their reactivities. *J. Mol. Catal. A-Chem.* **2002**, *180*, 293–298. [CrossRef]

12. Ashok, J.; Kathiraser, Y.; Ang, M.L.; Kawi, S. Bi-functional hydrotalcite-derived NiO–CaO–Al$_2$O$_3$ catalysts for steam reforming of biomass and/or tar model compound at low steam-to-carbon conditions. *Appl. Catal. B* **2015**, *172*, 116–128. [CrossRef]

13. Boroujerdnia, M.; Obeydavi, A. Synthesis and characterization of NiO/MgAl$_2$O$_4$ nanocrystals with high surface area by modified sol-gel method. *Microporous Mesoporous Mater.* **2016**, *228*, 289–296. [CrossRef]

14. Avcl, A.K.; Trimm, D.L.; Aksoylu, A.E.; Onsan, A. Hydrogen production by steam reforming of *n*-butane over supported Ni and Pt-Ni catalysts. *Appl. Catal. A.* **2004**, *258*, 235–240.

15. Ahn, K.; Choi, S.; Lee, J.; Kim, B.; Kim, J.; Kim, H. Enhanced carbon tolerance on Ni-based reforming catalyst with Ir alloying: A DFT study. *Appl. Surf. Sci.* **2017**, *419*, 678–682. [CrossRef]

16. Tian, H.; Li, X.; Chen, S.; Zeng, L.; Gong, J. Role of Sn in Ni-Sn/CeO$_2$ Catalysts for Ethanol Steam Reforming. *Chin. J. Chem.* **2017**, *35*, 651–658.

17. Wang, H.; Blaylock, W.; Dam, A.H.; Lilang, S.E.; Rout, K.R.; Zhu, Y.-A.; Green, W.H.; Homen, A.; Chen, D. Steam methane reforming on a Ni-based bimetallic catalyst: density functional theory and experimental studies of the catalytic consequence of surface alloying of Ni with Ag. *Catal. Sci. Technol.* **2017**, *7*, 1713–1715. [CrossRef]

18. Park, K.S.; Son, M.; Park, M.-J.; Kim, D.H.; Kim, J.H.; Park, S.H.; Choi, J.-H.; Bae, J.W. Adjusted interactions of nickel nanoparticles with cobalt-modified MgAl$_2$O$_4$-SiC for an enhanced catalytic stability during steam reforming of propane. *Appl. Catal. A* **2018**, *549*, 117–133. [CrossRef]

19. Resini, C.; Delgado, M.C.H.; Arrighi, L.; Alemany, L.J.; Marazza, R.; Busca, G. Propene versus propane steam reforming for hydrogen production over Pd-based and Ni-based catalysts. *Catal. Commun.* **2005**, *6*, 441–445. [CrossRef]

20. Anjaneyulu, C.; Costa, L.O.; Ribeiro, M.C.; Neto, R.C.; Mattos, L.V.; Venugopal, A.; Noronha, F.B. Effect of Zn addition on the performance of Ni/Al$_2$O$_3$ catalyst for steam reforming of ethanol. *Appl. Catal. A* **2016**, *519*, 85–98. [CrossRef]

21. Lee, G.; Kim, D.; Kwak, B.S.; Kang, M. Hydrogen rich production by ethanol steam reforming reaction over Mn/Co$_{10}$Si$_{90}$MCM-48 catalysts. *Catal. Today* **2014**, *232*, 139–150. [CrossRef]

22. Chen, A.; Yan, Y.; Elnashaie, S. Catalyst deactivation and engineering control for steam reforming of higher hydrocarbons in a novel membrane reformer. *Chem. Eng. Sci.* **2004**, *59*, 1965–1978. [CrossRef]

23. Ginsburg, J.M.; Piña, J.; Solh, T.E.; Lasa, H.I. Coke Formation over a Nickel Catalyst under Methane Dry Reforming Conditions: Thermodynamic and Kinetic Models. *Ind. Eng. Chem. Res.* **2005**, *44*, 4846–4854. [CrossRef]

24. Gao, F.; Tang, X.; Yi, H.; Zhao, X.; Li, C.; Li, J.; Shi, Y.; Meng, X. A Review on Selective Catalytic Reduction of NOx by NH$_3$ over Mn–Based Catalysts at Low Temperatures: Catalysts, Mechanisms, Kinetics and DFT Calculations. *Catalysts* **2017**, *7*, 1–32. [CrossRef]

25. Obata, S.; Kato, M.; Yokoyama, H.; Iwata, Y.; Kikumoto, Y.; Sakurada, O. Synthesis of nano CoAl$_2$O$_4$ pigment for ink-jet printing to decorate porcelain. *J. Ceram. Soc. Jpn.* **2011**, *119*, 208–213. [CrossRef]

26. Liu, K.; Schmedake, T.A.; Tsu, R. A comparative study of colloidal silica spheres: Photonic crystals versus Bragg's law. *Phys. Lett. A* **2008**, *372*, 4517–4520. [CrossRef]

27. Cepuritis, R.; Garboczi, E.J.; Ferraris, C.F.; Jacobsen, S.; Sorensen, B.E. Measurement of particle size distribution and specific surface area for crushed concrete aggregate fines. *Adv. Powder Technol.* **2017**, *28*, 706–720. [CrossRef]

28. Bakar, W.A.W.A.; Ali, R.; Mohammad, N.S. The effect of noble metals on catalytic methanation reaction over supported Mn/Ni oxide based catalysts. *Arab. J. Chem.* **2015**, *8*, 632–643. [CrossRef]

29. Takenaka, S.; Orita, Y.; Umebayashi, H.; Matsune, H.; Kishida, M. High resistance to carbon deposition of silica-coated Ni catalysts in propane stream reforming. *Appl. Catal. A* **2008**, *351*, 189–194. [CrossRef]

30. Wang, M.; Jin, L.; Li, Y.; Lv, J.; Wei, B.; Hu, H. In-situ catalytic upgrading of coal pyrolysis tar coupled with CO$_2$ reforming of methane over Ni-based catalysts. *Fuel Process. Technol.* **2018**, *177*, 119–128. [CrossRef]

31. Cordoba, M.; Miranda, C.; Lederhos, C.; Pascual, F.; Ardila, A.; Fuentes, G.A.; Pouilloux, Y.; Ramirez, A. Catalytic performance of Co$_3$O$_4$ on different activated carbon supports in the benzyl alcohol oxidation. *Catalysts* **2017**, *7*, 384–396. [CrossRef]

32. Petitto, S.C.; Langell, M.A. Surface composition and structure of Co_3O_4 (110) and the effect of impurity segregation. *J. Vac. Sci. Technol. A* **2004**, *22*, 1690–1697. [CrossRef]

33. Jin, J.; Park, J.; Shon, J.K.; Kim, J.H.; Li, Z.; Park, Y.; Kim, J.M. Low temperature CO oxidation over Pd catalysts supported on highly ordered mesoporous metal oxides. *Catal. Today* **2012**, *185*, 183–190. [CrossRef]

34. Ma, D.; Lu, Z.; Tang, Y.; Li, Y.; Tang, Z.; Yang, Z. Effect of lattice strain on the oxygen vacancy formation and hydrogen adsorption at CeO_2 (111) surface. *Phys. Lett. A* **2014**, *378*, 2570–2575. [CrossRef]

35. Kim, K.M.; Kwak, B.S.; Park, N.-K.; Lee, T.J.; Lee, S.T.; Kang, M. Effective hydrogen production from propane steam reforming over bimetallic co-doped $NiFe/Al_2O_3$ catalyst. *J. Ind. Eng. Chem.* **2017**, *46*, 324–336. [CrossRef]

36. Kim, J.; Samano, E.; Koel, B.E. CO Adsorption and Reaction on Clean and Oxygen-Covered Au (211) Surfaces. *J. Phys. Chem. B* **2006**, *110*, 17512–17517. [CrossRef] [PubMed]

37. Rao, G.R.; Mishra, B.G. Structural, redox and catalytic chemistry of ceria based materials. *Bull. Catal. Soc. India* **2003**, *2*, 122–134.

38. Bobrova, L.; Andreev, D.; Ivanov, E.; Mezentseva, N.; Simonov, M.; Makarshin, L.; Gribovskii, L.; Sadykov, V. Water–Gas Shift Reaction over Ni/CeO_2 Catalysts. *Catalysts* **2017**, *7*, 310–334. [CrossRef]

39. Noisong, P.; Danvirutai, C. Kinetics and Mechanism of Thermal Dehydration of $KMnPO_4 \cdot H_2O$ in a Nitrogen Atmosphere. *Ind. Eng. Chem. Res.* **2010**, *49*, 3146–3151. [CrossRef]

40. Li, Y.; Wang, X.; Xie, C.; Song, C. Influence of ceria and nickel addition to alumina-supported Rh catalyst for propane steam reforming at low temperatures. *Appl. Catal. A* **2009**, *357*, 213–222. [CrossRef]

41. Weerakkody, C.; Biswas, S.; Song, W.; He, J.; Wasalathanthri, N.; Dissanayake, S.; Kriz, D.A.; Dutta, B.; Sui, S.L. Controllable synthesis of mesoporous cobalt oxide for peroxide free catalytic epoxidation of alkenes under aerobic conditions. *Appl. Catal. B* **2018**, *221*, 681–690. [CrossRef]

42. Pieck, C.L.; Jablonski, E.L.; Parera, J.M. Recovering of the catalytic functions of naphtha reforming catalysts by partial coke burning. *Appl. Catal.* **1991**, *70*, 19–28. [CrossRef]

43. Mattos, L.V.; Rodino, E.; Resasco, D.E.; Passos, F.B.; Noronha, F.B. Partial oxidation and CO_2 reforming of methane on Pt/Al_2O_3, Pt/ZrO_2, and $Pt/Ce–ZrO_2$ catalysts. *Fuel Process. Technol.* **2003**, *83*, 147–161. [CrossRef]

44. Lu, W.; Iwasa, Y.; Ou, Y.; Jinno, D.; Kamiyama, S.; Petersen, P.M.; Ou, H. Effective optimization of surface passivation on porous silicon carbide using atomic layer deposited Al_2O_3. *RSC Adv.* **2017**, *7*, 8090–8097. [CrossRef]

45. Deng, S.; Li, S.; Li, H.; Zhang, Yi. Oxidative dehydrogenation of ethane to ethylene with CO_2 over $Fe-Cr/ZrO_2$ catalysts. *Ind. Eng. Chem. Res.* **2009**, *48*, 7561–7566. [CrossRef]

46. Xu, W.; He, H.; Yu, Y. Deactivation of a Ce/TiO_2 catalyst by SO_2 in the selective catalytic reduction of NO by NH_3. *J. Phys. Chem. C* **2009**, *113*, 4426–4432. [CrossRef]

47. Kulkarni, S.B.; Patil, U.M.; Shackery, I.; Sohn, J.S.; Lee, S.; Park, B.; Jun, S.C. High-performance supercapacitor electrode based on a polyaniline nanofibers/3D graphene framework as an efficient charge transporter. *J. Mater. Chem. A* **2014**, *2*, 498–4998. [CrossRef]

48. Do, J.Y.; Lee, J.H.; Park, N.-K.; Lee, T.J.; Lee, S.T.; Kang, M. Synthesis and characterization of $Ni_{2-x}Pd_xMnO_4/\gamma\text{-}Al_2O_3$ catalysts for hydrogen production via propane steam reforming. *Chem. Eng. J.* **2018**, *334*, 1668–1678. [CrossRef]

49. Jo, S.W.; Im, Y.; Do, J.Y.; Park, N.-K.; Lee, T.J.; Lee, S.T.; Cha, M.S.; Jeon, M.; Kang, M. Synergies between Ni, Co, and Mn ions in trimetallic $Ni_{1-x}Co_xMnO_4$ catalysts for effective hydrogen production from propane steam reforming. *Renew. Energy* **2017**, *113*, 248–256. [CrossRef]